

Ultralow Thermal Conductivity in Earth-Abundant $\text{Cu}_{1.6}\text{Bi}_{4.8}\text{S}_8$: Anharmonic Rattling of Interstitial Cu

Animesh Bhui, Moinak Dutta, Madhubanti Mukherjee, Kewal Singh Rana, Abhishek K. Singh, Ajay Soni, and Kanishka Biswas*

Cite This: *Chem. Mater.* 2021, 33, 2993–3001

Read Online

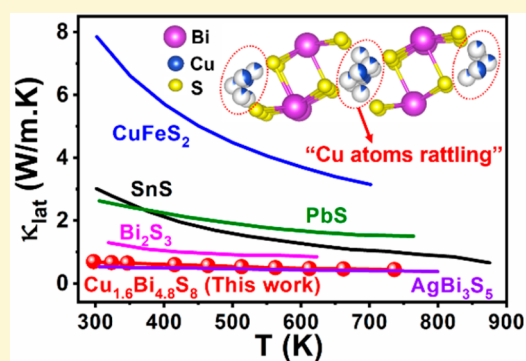
ACCESS |

Metrics & More

Article Recommendations

Supporting Information

ABSTRACT: Earth-abundant, nontoxic crystalline compounds with intrinsically low lattice thermal conductivity (κ_{lat}) are central to the development of thermoelectrics and thermal barrier coatings. Investigation of the fundamental origins of such low κ_{lat} and understanding its relationship with the chemical bonding and structure in solids thus stands paramount in order to furnish such low thermally conductive compounds. Herein, we synthesized earth-abundant, cost-effective, and nontoxic n-type ternary sulfide $\text{Cu}_{1.6}\text{Bi}_{4.8}\text{S}_8$, which exhibits an intrinsically ultralow κ_{lat} of ~ 0.71 – 0.44 W/m·K in the temperature range of 296–736 K. Structural analysis via atomic refinement unveiled large atomic displacement parameters (ADPs) for interstitial Cu clusters, demonstrating intrinsic rattling-like behavior. Electron localization function (ELF) analysis further shows that these rattling Cu atoms are weakly bonded and thus can generate low-energy Einstein vibrational modes. Low-temperature heat capacity (C_p) and temperature-dependent Raman spectra concord the presence of such low-energy optical modes. Density functional theory (DFT)-based phonon dispersions reveal that these low-lying optical phonons arise primarily due to the presence of chemical bonding hierarchy and simultaneous rattling of weakly bonded interstitial Cu atoms. These low-energy optical modes strongly scatter the heat-carrying acoustic phonons, thereby reducing the phonon lifetime to an ultrashort value (2–4.5 ps) and κ_{lat} to a very low value, which is lower than that of the many state-of-the-art metal sulfides.



INTRODUCTION

The discovery and development of environmentally benign materials for efficient thermoelectrics, thermal barrier coating, and refractories necessitates developing earth-abundant crystalline solids with low lattice thermal conductivity (κ_{lat}).^{1–5} Heat in crystalline solids is carried out using free charge carriers and lattice vibrations (phonons). While free charge carriers are essential for improving the electrical conductivity of a material, lattice thermal conductivity (κ_{lat}) provides an independent variable to control the thermoelectric figure of merit (zT).

Lowering of κ_{lat} is traditionally carried out via extrinsically perturbing the lattice using point defects,⁶ alloying,⁷ nanostructuring or grain-boundary engineering,⁸ multiscale hierarchical architectures, and mesoscale structuring.⁹ All of these aforementioned methods are efficient in scattering a wide range of phonon frequencies to lower the κ_{lat} sufficiently by decreasing the phonon lifetime but inevitably impose a devolving effect on carrier transport by scattering the charge carriers. Crystalline solids with inherently low κ_{lat} are thus regarded as an emerging alternative to achieve high-performance thermoelectrics, and understanding the impact of lattice dynamics on phonon transport becomes essential to developing novel materials that can intrinsically impede

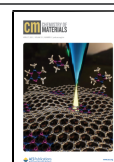
phonon flow.¹⁰ Although metal sulfides are known to show higher κ_{lat} compared to that of the selenides and tellurides due to the lighter mass of S, ultralow κ_{lat} in crystalline metal sulfides is desirable due to the low cost and high earth abundance of sulfur.

Intrinsically low κ_{lat} values in crystalline solids are seen in solids possessing complex crystal structures,^{11–13} a 2D-layered structure with substantial lattice anisotropy (e.g., BiSe, BiTe, SnSe, and SnS),^{14–19} liquid-like random ionic movement with a superionic lattice substructure resembling a “phonon glass-electron crystal (PGEC)”²⁰ (e.g., Cu_2S , Cu_{2-x}Se , and $\text{Cu}_{12}\text{Sb}_4\text{S}_{13}$),^{21–23} intrinsic rattling motion (e.g., $\text{Na}_{0.8}\text{CoO}_2$, Tl_3VSe_4 , TlSe , AgBi_3S_5 , TlInTe_2 , and CsAg_5Te_3),^{24–31} resonant bonding,³² ferroelectric instability,³³ heterogeneous bonding, and lone pair driven anharmonicity (e.g., AgPbBiSe_3 , AgSbTe_2 , CuBiS_2 , $\text{Cs}_2\text{PbI}_2\text{Cl}_2$, and AgBiS_2).^{34–39}

Received: February 23, 2021

Revised: March 26, 2021

Published: April 5, 2021



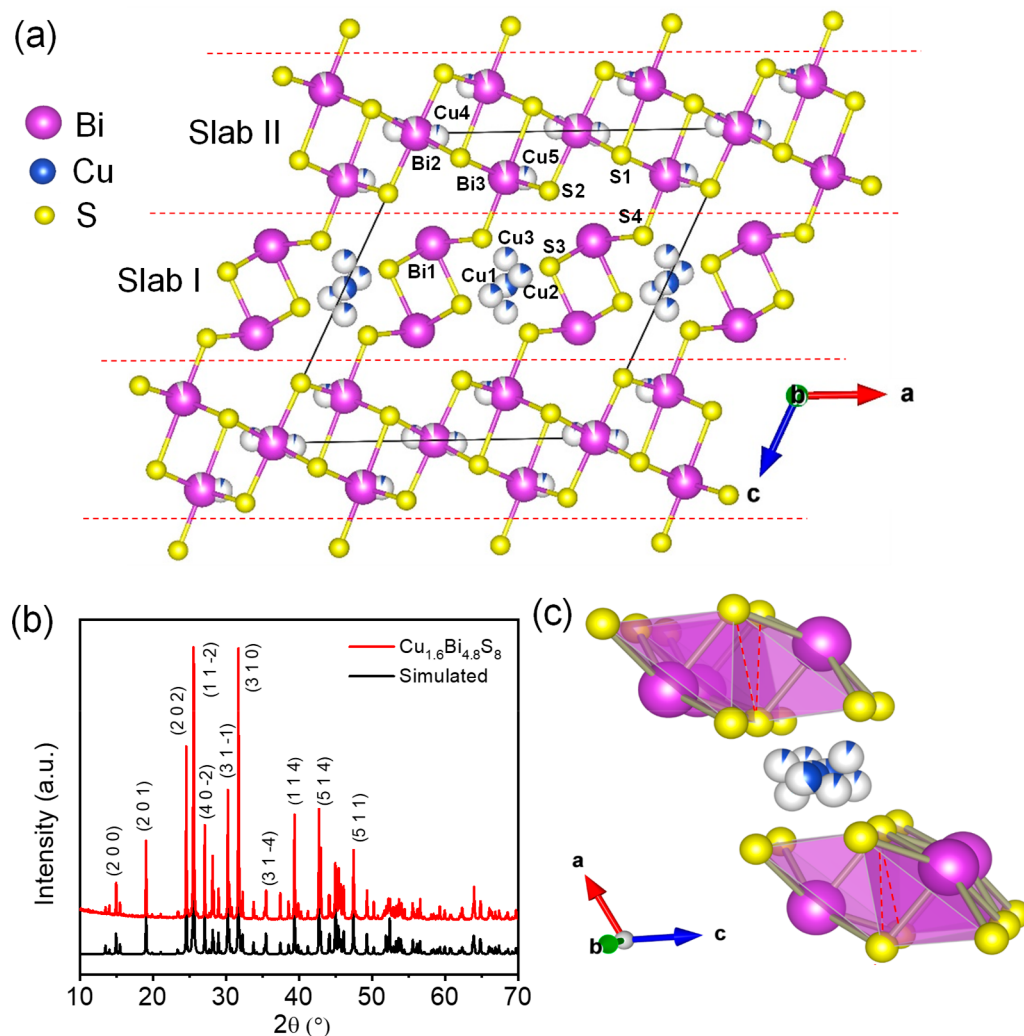


Figure 1. (a) Monoclinic structure of $\text{Cu}_{1.6}\text{Bi}_{4.8}\text{S}_8$ viewed along the b axis. Structure can be divided into two different types of slabs. (b) PXRD pattern of $\text{Cu}_{1.6}\text{Bi}_{4.8}\text{S}_8$. (c) Partial representation of square pyramidal Bi_3S_5 substructures with interstitial Cu clusters (Slab I). Shared face between two square pyramidal units is shown by dashed red-colored lines.

Although compounds with inherently low κ_{lat} values are fundamentally rich and overcome the problems that traditional phonon-scattering methods exhibit, utilizing them for mass-market application would require an earth-abundant, less expensive, and environmentally benign material. In this case, nontoxic metal sulfides are therefore viewed as an alternative and promising substitute to overcome such obstacles. Here, S, also being earth abundant and low cost as compared to Te and Se (Figure S1, Supporting Information, SI), provides long-term availability and price stability, and thus, significant attention has been diverted toward producing the next generation of intrinsically low κ_{lat} materials, which are primarily S based.^{12,19,21,27,38,40–51}

Herein, we investigate the origin of intrinsically low κ_{lat} (0.71–0.44 W/m·K in the temperature range of 296–736 K) of an eco-friendly and earth-abundant n -type $\text{Cu}_{1.6}\text{Bi}_{4.8}\text{S}_8$. The ultralow κ_{lat} measured in $\text{Cu}_{1.6}\text{Bi}_{4.8}\text{S}_8$ is indeed lower than that of many state of the art metal sulfides. $\text{Cu}_{1.6}\text{Bi}_{4.8}\text{S}_8$ adopts a monoclinic structure with seemingly two different substructures (Figure 1a) comprised of distinct chemical bonding environments. Structural analysis of $\text{Cu}_{1.6}\text{Bi}_{4.8}\text{S}_8$ revealed bonding hierarchy throughout the lattice with weakly bonded interstitial Cu clusters, which exhibits intrinsic rattling

dynamics, thus generating low-energy optical phonon modes. The presence of such low-energy modes has been verified through low-temperature heat capacity (C_p) and Raman spectroscopy measurements. Density functional theoretical calculations further shed light on the bonding of $\text{Cu}_{1.6}\text{Bi}_{4.8}\text{S}_8$, where we observed that the interstitial Cu atoms are weakly bonded with the surrounding S atoms. Phonon dispersion spectra revealed the presence of low-lying optical phonon modes, optical–acoustic phonon coupling, and significantly high anharmonicity (very large Grüneisen parameter ($\gamma > 15$)), all of which hinder the acoustic phonon propagation with an ultrashort phonon lifetime (2–4.5 ps), resulting in an ultralow κ_{lat} in $\text{Cu}_{1.6}\text{Bi}_{4.8}\text{S}_8$.

METHODS

Reagents. High-quality elemental copper (Alfa-Aesar, Cu, 99.999%), bismuth (Sigma-Aldrich, Bi, 99.999%), and sulfur (Alfa Aesar, S, 99.99%) were used, and no further purifications were done.

Synthesis. Crystalline ingot of $\text{Cu}_{1.6}\text{Bi}_{4.8}\text{S}_8$ was synthesized via stoichiometric mixing of high-quality constituent elements of Cu, Bi, and S in a quartz tube. The quartz ampule was vacuum sealed at $\sim 10^{-5}$ Torr. The tube was kept in a box furnace and gradually heated to 723 K in 7 h to minimize S evaporation and then to 1323 K in 6 h. The tube was then kept at 1323 K for 10 h with frequent shaking to

ensure sample homogeneity. Then the sample was cooled to 873 K over 5 h and annealed for 24 h followed by slow cooling to room temperature over 15 h. The as-synthesized sample was finely powdered using a mortar and pestle in an inert atmosphere glovebox, and spark plasma sintering (SPS) (SPS211-LX, Dr. Sinter Lab) was then performed to consolidate the sample. Powdered samples were filled into a graphite die (10 mm diameter) which was subjected to 450 °C under vacuum conditions ($\sim 10^{-3}$ Torr) in 5 min followed by a dwelling time of 10 min and subsequently cooled to room temperature (RT). The consolidation of the powder was done under 3.9 kN uniaxial pressure all through the sintering process. For transport properties measurement a cylindrical sample (~ 10 mm diameter, 12 mm height) was cut by a diamond saw followed by further polishing. The relative density of the SPS-processed sample was estimated to be >96% of the theoretical value.

Powder X-ray Diffraction (PXRD). A PANalytical diffractometer with Cu K α 1 ($\lambda = 1.54059$ Å) radiation was used to collect the powder XRD pattern at RT. Rietveld refinement was performed using the FullProf program.

Band Gap Measurement. The optical band gap of the finely powdered sample was estimated by diffuse reflectance spectroscopy (DRS) using a FT-IR Bruker IFS 66 V/S spectrometer in the wavelength scale of 6000–400 cm^{-1} at room temperature. From the reflectance (R) data, absorption (α/S) data were calculated using the Kubelka–Munk formula: $\alpha/S = (1 - R)^2/(2R)$, where α , S , and R correspond to absorption, scattering coefficient, and reflectance, respectively. The band gap was determined from the α/S vs E_g (eV) plot.

Thermal Conductivity. Laser flash analysis (LFA) was employed to measure the thermal diffusivity (D) of the sample in the temperature range of 296–736 K under N_2 atmosphere using a Netzsch LFA-457. Disc-shaped samples with dimensions of 10 mm \times 2 mm and a square-shaped sample with dimensions of 8 mm \times 8 mm \times 2 mm were used for measurement parallel (\parallel) and perpendicular (\perp) to the pressing (SPS) directions, respectively. Total thermal conductivity (κ) was then estimated using the formula $\kappa = DC_p\rho$, where C_p and ρ are the heat capacity considering the Dulong–Petit limit and density (>96%) of the sample, respectively. The experimental errors of all of the measured data obtained are within 5%. The electronic thermal conductivity (κ_{el}) was then subtracted from the total thermal conductivity (κ) to obtain the lattice thermal conductivity (κ_{lat}). κ_{el} was estimated using the Wiedemann–Franz law, $\kappa_{\text{el}} = L\sigma T$, where L , σ , and T are the Lorenz number, electrical conductivity, and temperature, respectively. L was calculated by considering the SPB (single parabolic band) model on the basis of fitting the temperature-dependent experimental Seebeck values.²⁶

A minimum thermal conductivity of ~ 0.347 W/m \cdot K was calculated using Cahill's formulation,⁵² that is $\kappa_{\text{min}} = 1.2 \ln^{(2/3)} \kappa_B v_S$, where n denotes the atomic number density, κ_B is the Boltzmann constant, and v_S is the average sound velocity estimated from heat capacity (C_p) measurements. A mean sound (v_S) velocity of ~ 1686 m/s is determined using the equation $\kappa_B \Theta_D = \hbar(6\pi^2 n)^{1/3} v_S$,⁵³ where Θ_D , \hbar , and n are the Debye temperature, reduced Planck constant, and number density of atoms, respectively.

Electrical Transport Properties. A ZEM-3 (ULVAC-RIKO) instrument was used to measure both the electrical conductivity (σ) and the Seebeck coefficients (S) concurrently in the temperature range of 296–736 K under He atmosphere. For the measurement, parallelepiped-shaped samples were used. The electrical and thermal transport properties were measured along the same pressing direction.

Hall Measurement. Hall measurement was done under a variable magnetic field of 0–1 T and a dc current of 90 mA at RT in an in-house set up developed by Excel Instrument. The carrier concentration (n) is measured to be $\sim 4.3 \times 10^{18}$ cm^{-3} . The carrier mobility is estimated to be ~ 220 (parallel to the SPS pressing direction) and ~ 209 $\text{cm}^2 \text{V}^{-1} \text{s}^{-1}$ (perpendicular to the SPS pressing direction).

Heat Capacity. The heat capacity (C_p) of $\text{Cu}_{1.6}\text{Bi}_{4.8}\text{S}_8$ was measured using a physical property measurement system (PPMS) by Quantum Design from 2 to 200 K.

Raman Spectroscopy. Raman measurements were conducted using a Jobin-Yvon Horiba LabRAM HR evolution Raman spectrometer with a Peltier-cooled CCD detector in back-scattering geometry using a 1800 gr/mm grating and 532 nm excitation wavelength (1.50 mW power) for a 20 s acquisition time. For observing low-lying Raman modes, which are close to the Rayleigh line, the ultralow-frequency filters are used. In addition, temperature-dependent Raman measurements were performed using a closed cycle cryostat (Montana Instruments) in the range of 4–200 K.

Computational Methods. All of the calculations were carried out using first-principles density functional theory as implemented in the Vienna ab initio simulation package (VASP). We used the projector augmented wave (PAW) potentials to represent the electron–ion interactions. The Perdew–Burke–Ernzerhof (PBE) functional within the generalized gradient approximation (GGA) was used to consider the electronic exchange and correlation. The optimized structure was achieved by employing a conjugate gradient scheme with the criteria of forces on individual atoms being less than 0.001 eV/Å. The second-order interatomic force constants were calculated by solving the phonon Boltzmann transport equation (PBTE) within Phonopy code using a supercell size of $1 \times 4 \times 1$. The group velocity and Grüneisen parameter were calculated using a similar supercell system and interatomic force constant. A strict energy convergence condition of 10^{-6} eV with an energy cutoff of 600 eV has been used to ensure the accuracy of the harmonic force constant.

The basic frame structure of the synthesized compound is monoclinic Bi_5S_8 . Adding Cu atoms into the interstitial position of the host framework does not alter the basic structure significantly, but substituting Cu atoms in place of Bi considerably perturbs the structure with a variation of occupancies. As it is quite complicated to accomplish theoretical calculations (DFT) with substituting atoms having fractional occupancies, we considered the most fundamental structure CuBi_5S_8 , as determined by Ohmasa et al.,⁵⁴ by taking care of charge neutrality. CuBi_5S_8 has interstitial Cu ions and a Bi_5S_8 framework. Therefore, the DFT-modeled structure does not include the substitution of Bi atoms by Cu atoms. We further used the modeled structure of CuBi_5S_8 for subsequent calculations. ELF has been calculated for three structures: the Bi_5S_8 framework, after adding Cu in the interstitial position, i.e., CuBi_5S_8 , and then $\text{Cu}_{1.6}\text{Bi}_{4.8}\text{S}_8$.

RESULTS AND DISCUSSION

A high-quality polycrystalline ingot of $\text{Cu}_{1.6}\text{Bi}_{4.8}\text{S}_8$, an earth-abundant metal sulfide,^{47–50} was synthesized via melting reaction in a sealed quartz tube at 1323 K and then densified into pellets using spark plasma sintering (SPS). It is a low band gap compound ~ 0.37 eV (Figure S2, SI) which crystallizes in a monoclinic structure (Figure 1a) having $C2/m$ space group. Figure 1b confirms the formation of pure $\text{Cu}_{1.6}\text{Bi}_{4.8}\text{S}_8$ with no second-phase impurities within the detection limit of the PXRD instrument. Rietveld refinement (Figure S3 and Table S1, SI) of the obtained PXRD data yielded lattice parameters values of $a = 13.2188$ (1) Å, $b = 4.0299$ (1) Å, $c = 14.0912$ (2) Å, $\alpha = \gamma = 90^\circ$, and $\beta = 115.5238$ (8) $^\circ$ and unit-cell volume = 677.38 (2) Å³.⁴⁷ $\text{Cu}_{1.6}\text{Bi}_{4.8}\text{S}_8$ possesses a complex crystal structure with seemingly two distinct alternating slabs (slab I and slab II) being interconnected to each other (Figure 1a). The complexity of the structure is illustrated by the fact that there are multiple Wyckoff positions in which these atoms reside. For simplicity, every element occupying a separate lattice has been assigned different numerical values. For example, the three bismuth positions are marked as Bi1, Bi2, and Bi3, five different Cu atoms are labeled as Cu1–Cu5, and four different S positions are labeled as S1–S4. Slab I consists of face-shared square pyramids of Bi_3S_5 substructures (comprised of Bi1, S3, and S4) along the crystallographic b direction where each S atom is shared between three Bi atoms (Figure 1c). Along the a direction, these square pyramidal

Bi_3S_5 substructures are separated via interstitial Cu atoms (Cu1, Cu2, and Cu3) having fractional occupancies (Figure 1c). These interstitial Cu atoms are weakly bonded and remain distributed along the *b* axis. Slab II consists of Bi atoms (Bi2 and Bi3) which are octahedrally surrounded by six S atoms (Figure 1a). The octahedra are connected via edge sharing. These Bi atoms are partially occupied and share its Wyckoff site with substitutional Cu atoms (Cu4 and Cu5). The occupancy of each atom obtained from Rietveld refinement is given in Table S1, SI. The presence of such contrasting substructures with interstitial disordered Cu atoms in slab I and positional disorder between Bi and Cu in slab II may lead to enhanced phonon–phonon scattering and subsequently lower the κ_{lat} in this compound.

$\text{Cu}_{1.6}\text{Bi}_{4.8}\text{S}_8$ exhibits a low total thermal conductivity (κ) of ~ 0.80 – 0.57 W/m·K in the temperature range of 296–736 K (Figure S4a, SI) both parallel (\parallel) and perpendicular (\perp) to the SPS pressing directions. κ_{lat} obtained by subtracting the electronic thermal conductivity (κ_{el}) estimated from the Weideman–Franz law ($\kappa_{\text{el}} = L\sigma T$, where L , σ , and T are the Lorenz number, electrical conductivity, and temperature, respectively) (Figure S4b, SI), from κ , has a ultralow value throughout the measured temperature range (296–736 K) (Figure 2a). We achieved similar κ_{lat} values both parallel (\parallel) and perpendicular (\perp) to the SPS pressing directions,

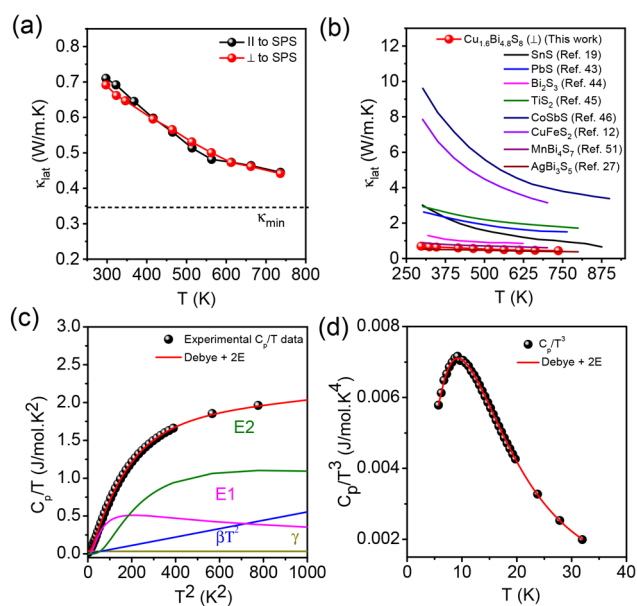


Figure 2. (a) Lattice thermal conductivity (κ_{lat}) of $\text{Cu}_{1.6}\text{Bi}_{4.8}\text{S}_8$ measured along the parallel (\parallel) and perpendicular (\perp) directions with respect to SPS pressing directions. (b) Comparison of κ_{lat} of $\text{Cu}_{1.6}\text{Bi}_{4.8}\text{S}_8$ with different metal sulfides (SnS,¹⁹ PbS,⁴³ Bi_2S_3 ,⁴⁴ TiS_2 ,⁴⁵ CoSbS ,⁴⁶ CuFeS_2 ,¹² MnBi_4S_7 ,⁵¹ and AgBi_3S_5 ,²⁷). (c) Debye–Einstein fit of C_p/T vs T^2 plot of $\text{Cu}_{1.6}\text{Bi}_{4.8}\text{S}_8$ with individual contributions from electronic (γ), Debye (β), and two Einstein modes (E_1 and E_2). (d) C_p/T^3 vs T plot shows a Boson-like peak feature and can be fitted solely by applying the combined Debye–Einstein model. In b, κ_{lat} data are adapted with permission from refs 19 (Copyright 2019 The American Association for the Advancement of Science), 43 (Copyright 2011 American Chemical Society), 44 (Copyright 2012 John Wiley and Sons), 45 (Copyright 2011 AIP Publishing), 46 (Copyright 2018 The Royal Society of Chemistry), 12 (Copyright 2019 American Chemical Society), 51 (Copyright 2019 John Wiley and Sons), and 27 (Copyright 2017 American Chemical Society).

indicating an isotropic structure of $\text{Cu}_{1.6}\text{Bi}_{4.8}\text{S}_8$ with three-dimensional (3D) connectivity. κ_{lat} decreases from ~ 0.71 W/m·K at 296 K to ~ 0.44 W/m·K at 736 K (Figure 2a), which is just above the theoretical minimum thermal conductivity ($\kappa_{\text{min}} = 0.347$ W/m·K) estimated from Cahill’s model for disordered crystals (see Methods).⁵² κ_{lat} of $\text{Cu}_{1.6}\text{Bi}_{4.8}\text{S}_8$ has an exceptionally low value compared with well-known metal sulfides (Figure 2b).

To elucidate the origin for such low κ_{lat} in $\text{Cu}_{1.6}\text{Bi}_{4.8}\text{S}_8$, we measured its low-temperature (2–200 K) heat capacity (C_p) (Figure S5, SI). Fitting a C_p/T vs T^2 plot using only the Debye model was found to be insufficient as the compound consists of weakly bonded interstitial Cu atoms which can vibrate rather independently, akin to Einstein oscillators. Thus, for proper analysis of the C_p/T vs T^2 plot, we applied the combined Debye–Einstein model,^{14,26} which is given as

$$\frac{C_p}{T} = \gamma + \beta T^2 + \sum_n \left(A_n (\Theta_{E_n})^2 (T^2)^{-3/2} \frac{e^{\Theta_{E_n}/T}}{(e^{\Theta_{E_n}/T} - 1)^2} \right) \quad (1)$$

The temperature-independent parameter γ in this Debye–Einstein model represents electronic contributions, while the second term $\beta = B(12\pi^4 N_A \kappa_B / 5)(\Theta_D)^{-3}$ corresponds to contributions arising from Debye modes. Here, κ_B , N_A , and Θ_D are the Boltzmann constant, Avogadro’s number, and the distinctive Debye temperature, respectively, and $B = 1 - \sum_n A_n / 3NR$, where R and N are the universal gas constant ($R = 8.314$ J mol⁻¹ K⁻¹) and the number of atoms for each formula unit, respectively. The last summation term in eq 1 accounts for the contribution originating from Einstein oscillators, where A_n corresponds to the Einstein prefactor for the n th Einstein mode, Θ_{E_n} . Figure 2c depicts the fitting for the C_p/T vs T^2 plot along with contributions from the individual parameters. The derived fitting parameters are presented in Table S3, SI. Two Einstein oscillator modes with characteristic temperatures of $\Theta_{E1} = 37.31$ K (~ 26 cm⁻¹) and $\Theta_{E2} = 74.21$ K (~ 51.5 cm⁻¹) were used for an accurate description of the data. These low-energy Einstein modes evidence for low-lying optical modes which couple with the acoustic phonons, thereby reducing the κ_{lat} of the material. A derived characteristic Debye temperature (Θ_D) of $\text{Cu}_{1.6}\text{Bi}_{4.8}\text{S}_8$ is found to be ~ 142 K. As above Θ_D , all of the phonon modes are excited; hence, lower Debye temperatures mean that the optical–acoustic phonon interaction originates at low temperature and thereby lowers κ_{lat} via a resistive Umklapp process.³⁹ A broad Boson-like hump is also observed in the C_p/T^3 vs T plot (Figure 2d), which is fitted by a combined Debye–Einstein model, affirming the presence of Einstein oscillator modes. We ascribe this Boson-like broad hump to the excess phonon density of states (PhDOS) originating due to the presence of low-frequency optical modes.²⁰

To comprehend the nature of chemical bonding in $\text{Cu}_{1.6}\text{Bi}_{4.8}\text{S}_8$, we performed electron localization function (ELF) analysis, which is the probability of finding a second electron having same spin in the vicinity of the first reference electron. Quantitatively, this probability is restricted to having possible values lies between 0 and 1. According to the color bar, ELF = 0, 0.5, and 1 correspond to complete delocalization (blue regions without electrons), a homogeneous electron distribution (green regions where the bonding is metallic), and perfect localization (red regions implying covalent bonds and the possibility of lone pairs).^{36,55,56} Electron localization

functions projected on the XZ plane [010] for Bi_5S_8 host matrix, CuBi_5S_8 , and $\text{Cu}_{1.6}\text{Bi}_{4.8}\text{S}_8$ (Figure 3a, 3b, and 3c) are

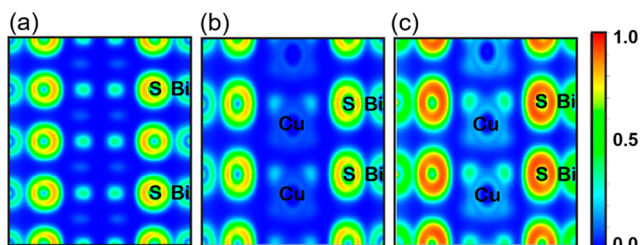


Figure 3. Electron localization function (ELF) projected on the XZ plane [010] of (a) Bi_5S_8 host system, (b) CuBi_5S_8 , and (c) $\text{Cu}_{1.6}\text{Bi}_{4.8}\text{S}_8$. Color bar represents the value of the ELF corresponding to different bondings.

calculated and compared to evaluate the variation of bonding with introducing Cu atoms at different positions. Figure 3a shows the ELF plot for the Bi_5S_8 host framework, where the green region between the Bi and the S atoms (corresponding to $\text{ELF} \approx 0.5$) indicates a strong localization around the atoms with larger electron localization around the S atoms. With the addition of only Cu interstitial atoms, delocalization around the Cu atoms is observed ($\text{ELF} \approx 0$) in CuBi_5S_8 , indicating a weak interaction between interstitial Cu and S, while localization around the S atoms increases more ($\text{ELF} \approx 0.7$) as compared to that of the Bi–S host framework (Figure 3b). ELF for $\text{Cu}_{1.6}\text{Bi}_{4.8}\text{S}_8$ (Figure 3c), which consists of substituted Cu atoms in the Bi position along with interstitial Cu atoms, exhibits complete electron delocalization ($\text{ELF} \approx 0$) around the Cu atoms for both the interstitial and the substitutional sites, even with stronger localization around S. The larger localization around the S atoms for each case can be attributed to the higher electronegativity of S. Since Cu is more electropositive as compared to Bi, with substitution of Cu, more charges get localized around S. Therefore, Cu incorporation results in bonding heterogeneity among the constituent elements. The delocalization around both types of Cu atoms (interstitial and substitutional) signifies the weaker interaction of Cu with the lattice framework, while larger localization around Bi–S leads to comparatively stronger bonding.

Weaker bonding of the Cu atoms in the lattice framework probably leads to the rattling of these atoms, which can generate low-energy Einstein modes as indicated via heat capacity measurements. To validate the presence of the rattling motion in these interstitial Cu clusters, we calculated the potential energy landscape with respect to the atomic displacement of each atom from their respective equilibrium positions of the modeled system CuBi_5S_8 where only interstitial Cu atoms are present for simplicity (Figure S6, SI). The corresponding plot, shown in Figure 4a, reveals that the Cu atoms show a shallow potential well, which signifies that these atoms are weakly bonded to the lattice, consistent with the large atomic displacement parameters (ADP) of interstitial Cu (Table S2, SI) and ELF analysis (Figure 3). Such a shallow potential well indicates that even with a little perturbation or thermal excitation these interstitial Cu atoms will rattle or vibrate from their equilibrium positions, thus inducing low-energy optical modes. Bi and S have a deeper potential energy surface, which is evidence of their comparatively stronger bonding character, corroborating with

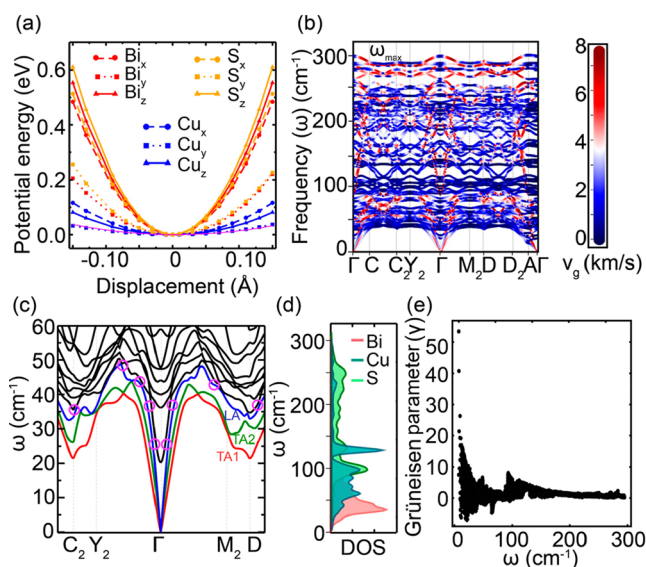


Figure 4. (a) Potential energy vs displacement plot, (b) phonon dispersion with corresponding group velocity (km/s), (c) zoomed view of phonon dispersion in the low-frequency region, (d) projected phonon density of states (PhDOS), and (e) mode Grüneisen parameter (γ) of CuBi_5S_8 .

the ELF analysis. Eigenvectors visualization (Figure S7a–f, SI) also indicates that the Cu atoms have larger vibrations than others, indicating an intrinsic rattling motion in the interstitial voids created by square pyramidal Bi_3S_5 substructures. The potential energy landscape shows that Cu in the y direction has the shallowest potential energy surface, thus indicating a larger rattling motion in the y direction, as compared to that of the x and z directions (Figure 4a).

To understand the mechanism of the low κ_{lat} , we performed density functional theory (DFT)-based phonon calculations in the modeled structure CuBi_5S_8 (only with interstitial Cu atoms). The absence of any imaginary frequencies in the total phonon dispersion of CuBi_5S_8 (Figure 4b) confirms the dynamic stability of CuBi_5S_8 (Figure S6, SI). Figure 4c shows the zoomed-in phonon dispersion of CuBi_5S_8 , where the first three low-frequency phonon modes are acoustic branches shown in red, green, and blue and the optical phonon branches are represented with black curves. From Figure 4c, several avoided crossings between the longitudinal acoustic (LA) phonon mode and the low-lying optical phonon modes within the frequency range of 20–50 cm^{-1} are observed (highlighted by magenta circles). The presence of such avoided crossing points implies a strong optical–acoustic hybridization arising due to the presence of soft vibrational optical modes.^{57,58} These hybridized modes are one of the signatures of rattling motion and lead to strong acoustic–optical phonon interaction, which aids in lowering the κ_{lat} in this material. The atom-projected phonon density of states (PhDOS) evidence that Bi and Cu mainly contribute to the low-frequency vibrational modes (Figure 4d), whereas high-frequency phonon modes are mostly dominated by lighter S atoms. The soft vibrations of the Cu atoms arise mostly due to its weak bonding character and rattling nature, whereas Bi due to its heavier atomic mass also contributes significantly to the low-frequency region. Bonding hierarchy along with avoided crossing of phonon modes suggest the presence of significant anharmonicity⁵⁷ in the lattice. To quantify this anharmonicity,

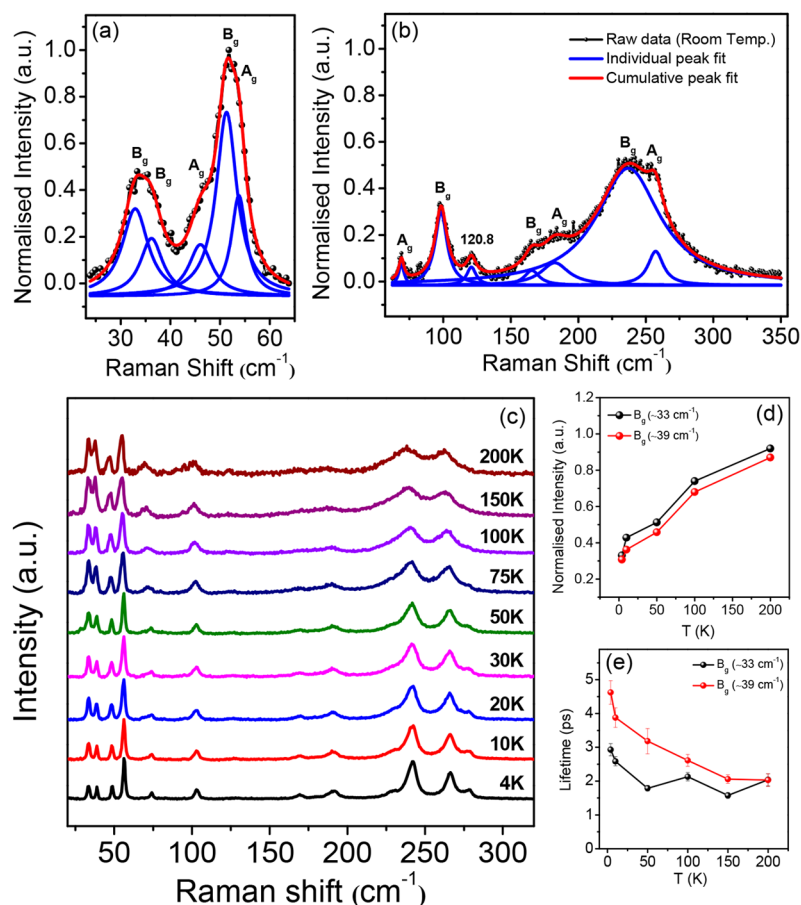


Figure 5. Room-temperature Raman spectra of $\text{Cu}_{1.6}\text{Bi}_{4.8}\text{S}_8$ in the spectral range (a) 20–65 and (b) 65–350 cm^{-1} . (c) Temperature-dependent Raman spectra from 4 to 200 K. (d) Temperature-dependent normalized intensity and (e) variation of phonon lifetime (ps) (with error bars) with the temperature for first two low-frequency Raman peaks.

we calculated the Grüneisen parameter (γ) with respect to the phonon frequency (Figure 4e). A considerably large value of γ (>15) in the 0–65 cm^{-1} region is observed, indicating significant anharmonicity in the lattice, which is mainly caused by the presence of bonding heterogeneity, rattling of interstitial Cu atoms, and the overall complexity in the structure.^{16,36,59} This large value of γ with high lattice anharmonicity also indicates enhanced phonon scattering and thereby reduces the lattice thermal conductivity (κ_{lat}).^{16,60}

The room-temperature Raman spectra of $\text{Cu}_{1.6}\text{Bi}_{4.8}\text{S}_8$ are shown in Figure 5a and 5b, where Figure 5a shows the Raman spectra from 20 to 65 cm^{-1} and Figure 5b shows the spectra from 65 to 350 cm^{-1} . The Raman modes are assigned as A_g and B_g symmetries from the DFT calculation of the modeled CuBi_5S_8 structure. At room temperature, we observed five A_g modes at ~ 46 , 53.8, 69, 182.6, and 257.3 cm^{-1} and six B_g modes at ~ 33 , 36.2, 51.3, 98.4, 165.6, and 237.1 cm^{-1} . We have not been able to assign the mode at ~ 120 cm^{-1} , which is probably related to substitutional Cu in $\text{Cu}_{1.6}\text{Bi}_{4.8}\text{S}_8$.^{61,62} The temperature-dependent (4–200 K) Raman spectra of $\text{Cu}_{1.6}\text{Bi}_{4.8}\text{S}_8$ are shown in Figure 5c (also see in Figure S8a–c, SI). With increasing the temperature from 4 to 200 K, most of the modes showed a red shift. The PhDOS indicates the low-frequency modes (from ~ 33 to 53.8 cm^{-1}) involve mainly the vibrations of Bi and weakly bonded interstitial Cu cations. Low-energy Einstein modes obtained from the low-temperature heat capacity measurement closely match with low-

energy Raman modes. These low-lying optical modes couple with the acoustic modes, resulting in a reduction of κ_{lat} significantly in $\text{Cu}_{1.6}\text{Bi}_{4.8}\text{S}_8$.^{26,63} The normalized intensity vs temperature plot (Figure 5d) of two low-frequency modes shows an increase in intensity with increasing temperature, indicating an increase of the phonon population. The higher phonon population causes phonon–phonon scattering, thereby lowering the κ_{lat} .^{26,37} The phonon lifetime (τ_i) ($\tau_i = \frac{1}{2\pi c(\text{fwhm})}$) estimated from the full width at half-maximum (fwhm) of the Raman peaks (~ 33 and 39 cm^{-1}) shows a decrease with increasing temperature (Figure 5e). We obtained a phonon lifetime in the range of 2–4.5 ps in $\text{Cu}_{1.6}\text{Bi}_{4.8}\text{S}_8$. As phonon scattering rates are inversely proportional to the phonon lifetime, such a short phonon lifetime rationalizes the presence of multiple phonon-scattering pathways that lead to an ultralow κ_{lat} value in $\text{Cu}_{1.6}\text{Bi}_{4.8}\text{S}_8$. The obtained phonon lifetime is much lower than that of a high thermally conductive material like MoS_2 (~ 38 ps at 300 K),⁶⁴ but the values are comparable with low thermally conductive perovskite halides and complex chalcogenides.^{37,65}

The electrical conductivity (σ) and Seebeck coefficient (S) of $\text{Cu}_{1.6}\text{Bi}_{4.8}\text{S}_8$ in the temperature range of 296–736 K are shown in Figure S9a and S9b (SI), respectively. The peak thermoelectric figure of merit (zT) of the compound is found to be 0.23 (parallel to the SPS pressing direction) and 0.26 (perpendicular to the SPS pressing direction) at 736 K (Figure

S9c, SI), which is reasonable in terms of pristine n-type metal sulfide.

CONCLUSIONS

$\text{Cu}_{1.6}\text{Bi}_{4.8}\text{S}_8$, a nontoxic, earth-abundant, narrow band gap degenerate semiconductor, exhibits an ultralow lattice thermal conductivity (κ_{lat}) of $\sim 0.71\text{--}0.44$ W/m·K in the temperature range of 296–736 K. $\text{Cu}_{1.6}\text{Bi}_{4.8}\text{S}_8$ shows intriguing structural variety consisting of the interstitial rattling of Cu atoms. Electron localization function analysis investigations indicate the presence of bonding hierarchy in $\text{Cu}_{1.6}\text{Bi}_{4.8}\text{S}_8$, where Cu atoms are weakly bonded, whereas Bi–S shows strong covalent interaction within them. Low-temperature heat capacity analysis reveals the existence of low-frequency optical phonon branches, which play a vital role in damping the heat flow by scattering the heat-carrying acoustic phonon branches. A temperature-dependent Raman study further confirms the presence of several low-frequency optical modes and phonon scattering via anharmonic coupling of acoustic and optical phonon modes, respectively. Theoretical analysis of the phonon dispersion indicated significant anharmonicity in the lattice and rattling of interstitial Cu atoms, which is also evident from a shallow potential well for Cu atoms compared to Bi and S. This synchronized constructive influence of the complex crystal structure, bonding heterogeneity, and intrinsic rattling atoms drastically affects the phonon propagation, thus resulting in an intrinsically ultralow κ_{lat} in $\text{Cu}_{1.6}\text{Bi}_{4.8}\text{S}_8$.

ASSOCIATED CONTENT

Supporting Information

The Supporting Information is available free of charge at <https://pubs.acs.org/doi/10.1021/acs.chemmater.1c00659>.

Abundance vs relative cost plot; band gap; Rietveld refinement; thermal transport properties; low- T heat capacity (C_p) plot; modeled structure; Eigenmode visualization; fitted Raman spectrum; electrical transport properties and zT ; tables for Rietveld refined structural parameters; Rietveld refined atomic displacement parameters (ADPs); C_p/T vs T^2 fitted parameters (PDF)

AUTHOR INFORMATION

Corresponding Author

Kanishka Biswas – New Chemistry Unit and School of Advanced Materials and International Centre of Materials Science, Jawaharlal Nehru Centre for Advanced Scientific Research (JNCASR), Bangalore 560064, India; orcid.org/0000-0001-9119-2455; Email: kanishka@jncasr.ac.in

Authors

Animesh Bhui – New Chemistry Unit, Jawaharlal Nehru Centre for Advanced Scientific Research (JNCASR), Bangalore 560064, India

Moinak Dutta – New Chemistry Unit, Jawaharlal Nehru Centre for Advanced Scientific Research (JNCASR), Bangalore 560064, India

Madhubanti Mukherjee – Materials Research Centre, Indian Institute of Science (IISc), Bangalore 560012, India

Kewal Singh Rana – School of Basic Sciences, Indian Institute of Technology Mandi, Mandi, Himachal Pradesh 175005, India

Abhishek K. Singh – Materials Research Centre, Indian Institute of Science (IISc), Bangalore 560012, India; orcid.org/0000-0002-7631-6744

Ajay Soni – School of Basic Sciences, Indian Institute of Technology Mandi, Mandi, Himachal Pradesh 175005, India; orcid.org/0000-0002-8926-0225

Complete contact information is available at: <https://pubs.acs.org/doi/10.1021/acs.chemmater.1c00659>

Notes

The authors declare no competing financial interest.

ACKNOWLEDGMENTS

A.B. thanks the CSIR for the fellowship. M.D. thanks UGC for the fellowship. K.B. acknowledges financial support from Swarnajayanti fellowship, Science and Engineering Research Board (SERB) (SB/SJF/2019-20/06), and Department of Science & Technology (DST) (DST/SJF/CSA-02/2018-19), India. A.K.S. and M.M. thankfully acknowledge support from the DST Ind-Korea grant. A.S. acknowledges the Science and Engineering Research Board (SERB) for funding (Grant No. CRG/2018/002197). A.K.S. and M.M. thank the Materials Research Centre and Supercomputer Education and Research Centre of the Indian Institute of Science for providing computing facilities. A.K.S. and M.M. acknowledge support from the Institute of Eminence (IoE) MHRD grant of the Indian Institute of Science.

REFERENCES

- (1) Tan, G.; Zhao, L.-D.; Kanatzidis, M. G. Rationally Designing High-Performance Bulk Thermoelectric Materials. *Chem. Rev.* **2016**, *116*, 12123–12149.
- (2) Sootsman, J. R.; Chung, D. Y.; Kanatzidis, M. G. New and Old Concepts in Thermoelectric Materials. *Angew. Chem., Int. Ed.* **2009**, *48*, 8616–8639.
- (3) Shi, X.-L.; Zou, J.; Chen, Z.-G. Advanced Thermoelectric Design: From Materials and Structures to Devices. *Chem. Rev.* **2020**, *120*, 7399–7515.
- (4) Xiao, Y.; Zhao, L.-D. Seeking new, highly effective thermoelectrics. *Science* **2020**, *367*, 1196–1197.
- (5) Pature, N. P.; Gell, M.; Jordan, E. H. Thermal barrier coatings for gas-turbine engine applications. *Science* **2002**, *296*, 280–284.
- (6) He, J.; Zhao, L.-D.; Zheng, J.-C.; Doak, J. W.; Wu, H.; Wang, H.-Q.; Lee, Y.; Wolverton, C.; Kanatzidis, M. G.; Dravid, V. P. Role of Sodium Doping in Lead Chalcogenide Thermoelectrics. *J. Am. Chem. Soc.* **2013**, *135*, 4624–4627.
- (7) Roychowdhury, S.; Biswas, R. K.; Dutta, M.; Pati, S. K.; Biswas, K. Phonon Localization and Entropy-Driven Point Defects Lead to Ultralow Thermal Conductivity and Enhanced Thermoelectric Performance in $(\text{SnTe})_{1-2x}(\text{SnSe})_x(\text{SnS})_x$. *ACS Energy Lett.* **2019**, *4*, 1658–1662.
- (8) Poudel, B.; Hao, Q.; Ma, Y.; Lan, Y.; Minnich, A.; Yu, B.; Yan, X.; Wang, D.; Muto, A.; Vashaee, D.; Chen, X.; Liu, J.; Dresselhaus, M. S.; Chen, G.; Ren, Z. High-Thermoelectric Performance of Nanostructured Bismuth Antimony Telluride Bulk Alloys. *Science* **2008**, *320*, 634–638.
- (9) Biswas, K.; He, J.; Blum, I. D.; Wu, C.-I.; Hogan, T. P.; Seidman, D. N.; Dravid, V. P.; Kanatzidis, M. G. High-performance bulk thermoelectrics with all-scale hierarchical architectures. *Nature* **2012**, *489*, 414–418.
- (10) Jana, M. K.; Biswas, K. Crystalline solids with intrinsically low lattice thermal conductivity for thermoelectric energy conversion. *ACS Energy Lett.* **2018**, *3*, 1315–1324.
- (11) Snyder, G. J.; Toberer, E. S. Complex thermoelectric materials. *Nat. Mater.* **2008**, *7*, 105–114.

- (12) Xie, H.; Su, X.; Zhang, X.; Hao, S.; Bailey, T. P.; Stoumpos, C. C.; Douvalis, A. P.; Hu, X.; Wolverton, C.; Dravid, V. P.; Uher, C.; Tang, X.; Kanatzidis, M. G. Origin of intrinsically low thermal conductivity in Tl_{17.6}Fe_{17.6}S₃₂ thermoelectric material: correlations between lattice dynamics and thermal transport. *J. Am. Chem. Soc.* **2019**, *141*, 10905–10914.
- (13) Pavan Kumar, V.; Guélou, G.; Lemoine, P.; Raveau, B.; Supka, A. R.; Al Rahal Al Orabi, R.; Fornari, M.; Suekuni, K.; Guilmeau, E. Copper-Rich Thermoelectric Sulfides: Size-Mismatch Effect and Chemical Disorder in the [TS₄]Cu₆ Complexes of Cu₂₆T₂Ge₆S₃₂ (T = Cr, Mo, W) Colusites. *Angew. Chem., Int. Ed.* **2019**, *58*, 15455–15463.
- (14) Samanta, M.; Pal, K.; Pal, P.; Waghmare, U. V.; Biswas, K. Localized Vibrations of Bi Bilayer Leading to Ultralow Lattice Thermal Conductivity and High Thermoelectric Performance in Weak Topological Insulator n-Type BiSe. *J. Am. Chem. Soc.* **2018**, *140*, 5866–5872.
- (15) Samanta, M.; Pal, K.; Waghmare, U. V.; Biswas, K. Intrinsically Low Thermal Conductivity and High Carrier Mobility in Dual Topological Quantum Material, n-Type BiTe. *Angew. Chem., Int. Ed.* **2020**, *59*, 4822–4829.
- (16) Zhao, L.-D.; Lo, S.-H.; Zhang, Y.; Sun, H.; Tan, G.; Uher, C.; Wolverton, C.; Dravid, V. P.; Kanatzidis, M. G. Ultralow thermal conductivity and high thermoelectric figure of merit in SnSe crystals. *Nature* **2014**, *508*, 373–377.
- (17) Chang, C.; Wu, M.; He, D.; Pei, Y.; Wu, C. F.; Wu, X.; Yu, H.; Zhu, F.; Wang, K.; Chen, Y.; Huang, L.; Li, J. F.; He, J.; Zhao, L. D. 3D charge and 2D phonon transports leading to high out-of-plane ZT in n-type SnSe crystals. *Science* **2018**, *360*, 778–783.
- (18) Lee, Y. K.; Luo, Z.; Cho, S. P.; Kanatzidis, M. G.; Chung, I. Surface Oxide Removal for Polycrystalline SnSe Reveals Near-Single-Crystal Thermoelectric Performance. *Joule* **2019**, *3*, 719–731.
- (19) He, W.; Wang, D.; Wu, H.; Xiao, Y.; Zhang, Y.; He, D.; Feng, Y.; Hao, Y.-J.; Dong, J.-F.; Chetty, R.; Hao, L.; Chen, D.; Qin, J.; Yang, Q.; Li, X.; Song, J.-M.; Zhu, Y.; Xu, W.; Niu, C.; Li, X.; Wang, G.; Liu, C.; Ohta, M.; Pennycook, S. J.; He, J.; Li, J.-F.; Zhao, L.-D. High thermoelectric performance in low-cost Sn_{0.91}Se_{0.09} crystals. *Science* **2019**, *365*, 1418–1424.
- (20) Takabatake, T.; Suekuni, K.; Nakayama, T.; Kaneshita, E. Phonon-glass electron-crystal thermoelectric clathrates: Experiments and theory. *Rev. Mod. Phys.* **2014**, *86*, 669–712.
- (21) He, Y.; Day, T.; Zhang, T.; Liu, H.; Shi, X.; Chen, L.; Snyder, G. J. High thermoelectric performance in non-toxic earth-abundant copper sulfide. *Adv. Mater.* **2014**, *26*, 3974–3978.
- (22) Liu, H.; Shi, X.; Xu, F.; Zhang, L.; Zhang, W.; Chen, L.; Li, Q.; Uher, C.; Day, T.; Snyder, G. J. Copper ion liquid-like thermoelectrics. *Nat. Mater.* **2012**, *11*, 422–425.
- (23) Xia, Y.; Ozoliņš, V.; Wolverton, C. Microscopic Mechanisms of Glasslike Lattice Thermal Transport in Cubic Cu₁₂Sb₄S₁₃ Tetrahedrites. *Phys. Rev. Lett.* **2020**, *125*, 085901.
- (24) Voneshen, D. J.; Refson, K.; Borissenko, E.; Krisch, M.; Bosak, A.; Piovano, A.; Cemal, E.; Enderle, M.; Gutmann, M. J.; Hoesch, M.; Roger, M.; Gannon, L.; Boothroyd, A. T.; Uthayakumar, S.; Porter, D. G.; Goff, J. P. Suppression of thermal conductivity by rattling modes in thermoelectric sodium cobaltate. *Nat. Mater.* **2013**, *12*, 1028–1032.
- (25) Mukhopadhyay, S.; Parker, D. S.; Sales, B. C.; Puzos, A. A.; McGuire, M. A.; Lindsay, L. Two-channel model for ultralow thermal conductivity of crystalline Tl₃VSe₄. *Science* **2018**, *360*, 1455–1458.
- (26) Dutta, M.; Matteppanavar, S.; Prasad, M. V. D.; Pandey, J.; Warankar, A.; Mandal, P.; Soni, A.; Waghmare, U. V.; Biswas, K. Ultralow Thermal Conductivity in Chain-like TlSe Due to Inherent Tl⁺ Rattling. *J. Am. Chem. Soc.* **2019**, *141*, 20293–20299.
- (27) Tan, G.; Hao, S.; Zhao, J.; Wolverton, C.; Kanatzidis, M. G. High thermoelectric performance in electron-doped AgBi₃S₅ with ultralow thermal conductivity. *J. Am. Chem. Soc.* **2017**, *139*, 6467–6473.
- (28) Dutta, M.; Samanta, M.; Ghosh, T.; Voneshen, D. J.; Biswas, K. Evidence of Highly Anharmonic Soft Lattice Vibrations in Zintl Rattler. *Angew. Chem., Int. Ed.* **2021**, *60*, 4259–4265.
- (29) Pal, K.; Xia, Y.; Wolverton, C. Microscopic mechanism of unusual lattice thermal transport in TlInTe₂. *npj Comput. Mater.* **2021**, *7*, 5.
- (30) Lin, H.; Tan, G.; Shen, J.-N.; Hao, S.; Wu, L.-M.; Calta, N.; Malliakas, C.; Wang, S.; Uher, C.; Wolverton, C.; Kanatzidis, M. G. Concerted Rattling in CsAg₃Te₃ Leading to Ultralow Thermal Conductivity and High Thermoelectric Performance. *Angew. Chem., Int. Ed.* **2016**, *55*, 11431–11436.
- (31) Lee, W.; Li, H.; Wong, A. B.; Zhang, D.; Lai, M.; Yu, Y.; Kong, Q.; Lin, E.; Urban, J. J.; Grossman, J. C.; Yang, P. Ultralow thermal conductivity in all-inorganic halide perovskites. *Proc. Natl. Acad. Sci. U. S. A.* **2017**, *114*, 8693–8697.
- (32) Lee, S.; Esfarjani, K.; Luo, T.; Zhou, J.; Tian, Z.; Chen, G. Resonant bonding leads to low lattice thermal conductivity. *Nat. Commun.* **2014**, *5*, 3525.
- (33) Sarkar, D.; Ghosh, T.; Roychowdhury, S.; Arora, R.; Sajan, S.; Sheet, G.; Waghmare, U. V.; Biswas, K. Ferroelectric Instability Induced Ultralow Thermal Conductivity and High Thermoelectric Performance in Rhombohedral p-Type GeSe Crystal. *J. Am. Chem. Soc.* **2020**, *142*, 12237–12244.
- (34) Dutta, M.; Pal, K.; Waghmare, U. V.; Biswas, K. Bonding heterogeneity and lone pair induced anharmonicity resulted in ultralow thermal conductivity and promising thermoelectric properties in n-type AgPbBiSe₃. *Chem. Sci.* **2019**, *10*, 4905–4913.
- (35) Morelli, D. T.; Jovic, V.; Heremans, J. P. Intrinsically Minimal Thermal Conductivity in Cubic I-V-VI₂ Semiconductors. *Phys. Rev. Lett.* **2008**, *101*, 035901.
- (36) Feng, Z.; Jia, T.; Zhang, J.; Wang, Y.; Zhang, Y. Dual effects of lone-pair electrons and rattling atoms in CuBiS₂ on its ultralow thermal conductivity. *Phys. Rev. B: Condens. Matter Mater. Phys.* **2017**, *96*, 235205.
- (37) Acharyya, P.; Ghosh, T.; Pal, K.; Kundu, K.; Singh Rana, K.; Pandey, J.; Soni, A.; Waghmare, U. V.; Biswas, K. Intrinsically Ultralow Thermal Conductivity in Ruddlesden-Popper 2D Perovskite Cs₂PbI₂Cl₂: Localized Anharmonic Vibrations and Dynamic Octahedral Distortions. *J. Am. Chem. Soc.* **2020**, *142*, 15595–15603.
- (38) Rathore, E.; Juneja, R.; Culver, S. P.; Minafra, N.; Singh, A. K.; Zeier, W. G.; Biswas, K. Origin of Ultralow Thermal Conductivity in n-Type Cubic Bulk AgBiS₂: Soft Ag Vibrations and Local Structural Distortion Induced by the Bi 6s² Lone Pair. *Chem. Mater.* **2019**, *31*, 2106–2113.
- (39) Nielsen, M. D.; Ozolins, V.; Heremans, J. P. Lone pair electrons minimize lattice thermal conductivity. *Energy Environ. Sci.* **2013**, *6*, 570–578.
- (40) Ge, Z.-H.; Zhao, L.-D.; Wu, D.; Liu, X.; Zhang, B.-P.; Li, J.-F.; He, J. Low-cost, abundant binary sulfides as promising thermoelectric materials. *Mater. Today* **2016**, *19*, 227–239.
- (41) Powell, A. V. Recent developments in Earth-abundant copper-sulfide thermoelectric materials. *J. Appl. Phys.* **2019**, *126*, 100901.
- (42) Lu, X.; Morelli, D. T.; Xia, Y.; Zhou, F.; Ozolins, V.; Chi, H.; Zhou, X.; Uher, C. High performance thermoelectricity in earth-abundant compounds based on natural mineral tetrahedrites. *Adv. Energy Mater.* **2013**, *3*, 342–348.
- (43) Johnsen, S.; He, J.; Androulakis, J.; Dravid, V. P.; Todorov, I.; Chung, D. Y.; Kanatzidis, M. G. Nanostructures boost the thermoelectric performance of PbS. *J. Am. Chem. Soc.* **2011**, *133*, 3460–3470.
- (44) Biswas, K.; Zhao, L. D.; Kanatzidis, M. G. Tellurium-Free Thermoelectric: The Anisotropic n-Type Semiconductor Bi₂S₃. *Adv. Energy Mater.* **2012**, *2*, 634–638.
- (45) Guilmeau, E.; Bréard, Y.; Maignan, A. Transport and thermoelectric properties in Copper intercalated TiS₂ chalcogenide. *Appl. Phys. Lett.* **2011**, *99*, 052107.
- (46) You, Y.; Su, X.; Hao, S.; Liu, W.; Yan, Y.; Zhang, T.; Zhang, M.; Wolverton, C.; Kanatzidis, M. G.; Tang, X. Ni and Se co-doping increases the power factor and thermoelectric performance of CoSbS. *J. Mater. Chem. A* **2018**, *6*, 15123–15131.

- (47) Tomeoka, K.; Ohmasa, M.; Sadanaga, R. Crystal chemical studies on some compounds in the $\text{Cu}_2\text{S}-\text{Bi}_2\text{S}_3$ system. *Mineral. J.* **1980**, *10*, 57–70.
- (48) Hwang, J.-Y.; Oh, M.-W.; Lee, K. H.; Kim, S. W. Strong correlation between the crystal structure and the thermoelectric properties of pavonite homologue $\text{Cu}_{x+y}\text{Bi}_{1-y}\text{Ch}_8$ (Ch = S or Se) compounds. *J. Mater. Chem. C* **2015**, *3*, 11271–11285.
- (49) Ahn, J. Y.; Hwang, J.-Y.; Ryu, B. K.; Oh, M.-W.; Lee, K. H.; Kim, S. W. Importance of crystal chemistry with interstitial site determining thermoelectric transport properties in pavonite homologue Cu-Bi-S compounds. *CrystEngComm* **2016**, *18*, 1453–1461.
- (50) Hwang, J.-Y.; Ahn, J. Y.; Lee, K. H.; Kim, S. W. Structural optimization for thermoelectric properties in Cu-Bi-S pavonite compounds. *J. Alloys Compd.* **2017**, *704*, 282–288.
- (51) Labégorre, J.-B.; Virfeu, A.; Bourhim, A.; Willeman, H.; Barbier, T.; Appert, F.; Juraszek, J.; Malaman, B.; Huguenot, A.; Gautier, R.; Nassif, V.; Lemoine, P.; Prestipino, C.; Elkaim, E.; Pautrot-D'Alençon, L.; Le Mercier, T.; Maignan, A.; Al Rahal Al Orabi, R.; Guilmeau, E. XBi_4S_7 (X = Mn, Fe): New Cost-Efficient Layered n-Type Thermoelectric Sulfides with Ultralow Thermal Conductivity. *Adv. Funct. Mater.* **2019**, *29*, 1904112.
- (52) Cahill, D. G.; Watson, S. K.; Pohl, R. O. Lower limit to the thermal conductivity of disordered crystals. *Phys. Rev. B: Condens. Matter Mater. Phys.* **1992**, *46*, 6131.
- (53) Agne, M. T.; Hanus, R.; Snyder, G. J. Minimum thermal conductivity in the context of diffuson-mediated thermal transport. *Energy Environ. Sci.* **2018**, *11*, 609–616.
- (54) Ohmasa, M.; Nowacki, W. The crystal structure of synthetic CuBi_3S_8 . *Z. Kristallogr. - Cryst. Mater.* **1973**, *137*, 422–432.
- (55) Savin, A.; Nesper, R.; Wengert, S.; Fässler, T. F. ELF: The electron localization function. *Angew. Chem., Int. Ed. Engl.* **1997**, *36*, 1808–1832.
- (56) Koumpouras, K.; Larsson, J. A. Distinguishing between chemical bonding and physical binding using electron localization function (ELF). *J. Phys.: Condens. Matter* **2020**, *32*, 315502.
- (57) Christensen, M.; Abrahamsen, A. B.; Christensen, N. B.; Juranyi, F.; Andersen, N. H.; Lefmann, K.; Andreasson, J.; Bahl, C. R. H.; Iversen, B. B. Avoided crossing of rattler modes in thermoelectric materials. *Nat. Mater.* **2008**, *7*, 811–815.
- (58) Li, W.; Carrete, J.; Madsen, G. K. H.; Mingo, N. Influence of the optical-acoustic phonon hybridization on phonon scattering and thermal conductivity. *Phys. Rev. B: Condens. Matter Mater. Phys.* **2016**, *93*, 205203.
- (59) Zhang, Y.; Skoug, E.; Cain, J.; Ozoliņš, V.; Morelli, D.; Wolverton, C. First-principles description of anomalously low lattice thermal conductivity in thermoelectric Cu-Sb-Se ternary semiconductors. *Phys. Rev. B: Condens. Matter Mater. Phys.* **2012**, *85*, 054306.
- (60) Singh, N. K.; Soni, A. Crystalline anharmonicity and ultralow thermal conductivity in layered Bi_2GeTe_4 for thermoelectric applications. *Appl. Phys. Lett.* **2020**, *117*, 123901.
- (61) Zhao, Y.; Chua, K. T. E.; Gan, C. K.; Zhang, J.; Peng, B.; Peng, Z.; Xiong, Q. Phonons in Bi_2S_3 nanostructures: Raman scattering and first-principles studies. *Phys. Rev. B: Condens. Matter Mater. Phys.* **2011**, *84*, 205330.
- (62) Houck, D. W.; Assaf, E. I.; Shin, H.; Greene, R. M.; Pernik, D. R.; Korgel, B. A. Pervasive Cation Vacancies and Antisite Defects in Copper Indium Diselenide (CuInSe_2) Nanocrystals. *J. Phys. Chem. C* **2019**, *123*, 9544–9551.
- (63) Acharya, S.; Pandey, J.; Soni, A. Enhancement of Power Factor for Inherently Poor Thermal Conductor Ag_8GeSe_6 by Replacing Ge with Sn. *ACS Appl. Energy Mater.* **2019**, *2*, 654–660.
- (64) Cai, Y.; Lan, J.; Zhang, G.; Zhang, Y.-W. Lattice vibrational modes and phonon thermal conductivity of monolayer MoS_2 . *Phys. Rev. B: Condens. Matter Mater. Phys.* **2014**, *89*, 035438.
- (65) Pandey, J.; Mukherjee, S.; Rawat, D.; Athar, S.; Rana, K. S.; Mallik, R. C.; Soni, A. Raman Spectroscopy Study of Phonon Liquid Electron Crystal in Copper Deficient Superionic Thermoelectric Cu_{2-x}Te . *ACS Appl. Energy Mater.* **2020**, *3*, 2175–2181.